On the Life Cycle of a Shallow Cumulus Cloud: Is It a Bubble or Plume, Active or Forced?

David M. Romps,[a,b] Rusen Öktem,[a,b] Satoshi Endo,[c] and Andrew M. Vogelmann[c]

[a] Department of Earth and Planetary Science, University of California, Berkeley, Berkeley, California
[b] Climate and Ecosystem Sciences Division, Lawrence Berkeley National Laboratory, Berkeley, California
[c] Environmental and Climate Sciences Department, Brookhaven National Laboratory, Upton, New York

ABSTRACT: A cloud's life cycle determines how its mass flux translates into cloud cover, thereby setting Earth's albedo. Here, an attempt is made to quantify the most basic aspects of the life cycle of a shallow cumulus cloud: the degree to which it is a bubble or a plume, and active or forced. Quantitative measures are proposed for these properties, which are then applied to hundreds of shallow cumulus clouds in Oklahoma using data from stereo cameras, a Doppler lidar, and large-eddy simulations. The observed clouds are intermediate between active and forced, but behave more like bubbles than plumes. The simulated clouds, on the other hand, are more active and plumelike, suggesting room for improvement in the modeling of shallow cumulus.

KEYWORDS: Cloud cover; Convective-scale processes; Cumulus clouds

1. Introduction

Although they are small, shallow cumulus clouds are so commonplace that they make an important contribution to Earth's albedo. By one estimate, cumulus clouds are responsible for $4.6\,\mathrm{W\,m^{-2}}$ of upwelling top-of-atmosphere radiative flux (Chen et al. 2000), without which Earth would warm by several degrees. To understand the radiative impact of shallow cumulus clouds from first principles, or even just well enough to represent it accurately in models, we must connect the dots from cloud-base mass flux to cloud-layer area fraction. In other words, we must understand the cloud's life cycle, i.e., how a mass of air moving up through the lifting condensation level translates to an amount and duration of cloudy air. As a small step in that direction, this paper suggests a way to quantify two basic aspects of that life cycle: bubble versus plume and active versus forced.

Stull (1985) introduced a classification system for cumulus clouds in which "active" clouds reach their level of free convection and "forced" clouds do not. (A third category called "passive" clouds was defined to be the decaying remnants of active clouds, but those will be treated as part of the active category here.) In that classification scheme, an active cloud is one that achieves positive buoyancy (determined in the field by visual identification of a rising turret), and a forced cloud is one that does not.

In the 1950s, it became increasingly clear that the updrafts of buoyant air in the boundary layer—referred to as thermals in recognition of their temperature anomaly—are more episodic than steady state (Yates 1953; Scorer and Ludlam 1953). Subsequently, the term "thermal" came to mean a transient bubble of rising, buoyant air, as distinguished from the term "plume" referring to a steady-state current of rising, buoyant air (Turner 1962; McCarthy 1974). Here, however, we will use the more precise and descriptive term of "bubble" instead of

"thermal." In this paper, we explore whether the ideas of forced, active, bubble, and plume can be made quantitively rigorous when applied to shallow cumulus clouds.

By the definitions of Stull (1985), the question of forced or active is a binary one: either no part of the cloud achieves positive buoyancy, or some part does. For our purposes, we need a more continuous measure. Note that a parcel of cloudy air that always has negative buoyancy will tend to sink back down through the cloud base. Alternatively, a parcel of cloudy air that achieves positive buoyancy will have a level of neutral buoyancy above the cloud base, so it will tend to stay above that level. Accordingly, we will redefine forced and active as the endpoints of a continuous variable F defined as the fraction of the cloud's mass that sinks back down through the cloud base.

Like forced and active, the standard definitions of bubble and plume are binary: either the convection is transient or steady state. To develop a more continuous measure, note that the instantaneous volume of a bubble is representative of the total volume of fluid involved in convecting over its life cycle. In contrast, the finite volume of a steady-state plume is not representative of the volume of fluid that convects through it, which is infinite in the case of an ideal plume that lasts forever. Accordingly, we will redefine bubble and plume as the endpoints of a continuous variable B defined as the largest instantaneous mass of the cloud divided by the total mass that convects into it.

2. Metrics

Since the shallow clouds studied here have thicknesses about 10% or less of the atmosphere's scale height, we can treat Lagrangian air volume as conserved. It would be straightforward to rewrite the equations in terms of mass, but doing so would gain little in accuracy at the expense of a more complicated notation.

For each cumulus cloud, imagine that we can measure the volume of air that ascends through its base during its lifetime
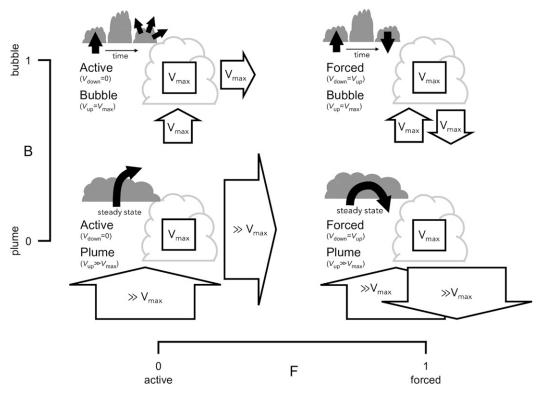
FIG. 1. The four extreme cases of a shallow cumulus cloud: (top left) an active bubble with $F \equiv V_{\mathrm{down}}/V_{\mathrm{up}} = 0$ and $B \equiv V_{\mathrm{max}}/V_{\mathrm{up}} = 1$, (top right) a forced bubble with $F = 1$ and $B = 1$, (bottom left) an active plume with $F = 0$ and $B = 0$, and (bottom right) a forced plume with $F = 1$ and $B = 0$.

(V_{up}), the volume of air that descends through its base during its lifetime (V_{down}), and the maximum instantaneous volume of the cloud during its lifetime (V_{max}). For shallow cumuli, these three parameters are enough to tell us the degree to which clouds are forced, active, bubble, and plume.

Consider a shallow cloud that behaves as a forced bubble: the bubble of subcloud air first rises above its lifting condensation level (LCL) and then sinks back down. To the extent that we can ignore entrainment (see below), then we know that V_{down} equals V_{up}. And, since a bubble's ascent and descent are sequential, V_{max} equals V_{up}. Therefore, we define a forced bubble to have both $V_{\mathrm{down}}/V_{\mathrm{up}}$ and $V_{\mathrm{max}}/V_{\mathrm{up}}$ equal to one. This case is depicted in the top-right panel of Fig. 1.

Next, consider a shallow cloud that behaves as an active plume: this cloud has a steady-state flux of air up through the LCL that is continuously detrained out the top and sides of the cloud's boundary. Because this cloud is in a steady state, V_{max} is vanishingly small compared to V_{up} over the cloud's effectively infinite lifetime, so $V_{\mathrm{max}}/V_{\mathrm{up}}$ is zero. And, because no air descends back down to the cloud's original LCL (i.e., the cloud base) as cloudy air, $V_{\mathrm{down}}/V_{\mathrm{up}}$ is zero. This case is depicted in the bottom-left panel of Fig. 1.

Two other extreme cases are an active bubble (top-left panel of Fig. 1) and a forced plume (bottom-right panel of Fig. 1). In between those four corners is a continuous two-dimensional phase space of clouds that are in between active and forced, and in between a bubble and a plume. All of the possibilities

can be quantified using F and B (for forced and bubble, respectively):

$$F = \frac{V_{\mathrm{down}}}{V_{\mathrm{up}}}, \qquad (1)$$

$$B = \frac{V_{\mathrm{max}}}{V_{\mathrm{up}}}. \qquad (2)$$

Likewise, we can measure the degree to which a cloud is active (A) or a plume (P) by $A = 1 - F$ and $P = 1 - B$. We should expect individual clouds to have $0 \leq F \leq 1$ and $0 \leq B \leq 1$.

Impact of entrainment

A potential concern is that convective entrainment would affect V_{down} and V_{max}, complicating the interpretation of F and B. For example, if part of the cloud were to entrain before sinking back down through the cloud base, that would impart a high bias to V_{down} and, therefore, to F, potentially giving even $F > 1$. Similarly, entrainment could bias V_{max} and, therefore, B to larger values, potentially giving even $B > 1$. Fortunately, these two biases are not expected to be of practical significance for shallow cumulus.

First, consider V_{down}. By choosing the cloud's initial LCL as the height over which we measure vertical volume fluxes through the clear–cloud interface, we are nearly guaranteed that a parcel of air passing downward through a clear–cloud interface at that level has not entrained; if it had, that parcel

would have a higher LCL and so would not generate a clear–cloud interface at the cloud's initial LCL. Instead, the parcel would convert from cloudy to clear at a height above the cloud base and so would be recorded as having detrained in the cloud layer with our definitions of V_{down} and V_{up}. Note that this comports with the standard definition of ''detrain'' as the conversion of a parcel of air from cloudy to clear (Siebesma and Holtslag 1996; Romps 2010; Dawe and Austin 2011).

Second, consider V_{max}. A cloud can puff up its volume by entraining clear air, but only to a point: if the cloud entrains too much, it will evaporate all of its droplets and cease to be a cloud. Using a snapshot of shallow cumulus from one of the large-eddy simulations, we calculate in the appendix the maximum factor by which each cloud could puff up by entrainment, and we find values with a mean of 1.19 and a standard deviation of 0.06. Note that these are not the *actual* puff factors, but the theoretical maxima. Therefore, we infer that the likely actual puff factors are ≲10%, and such errors are small enough to be ignored in the analysis done here.

3. Data

The primary sources of data for this study are four-dimensional cloud reconstructions using stereo photogrammetry (section 3a), measurements of cloud-base vertical velocity using a Doppler lidar (section 3b), and large-eddy simulations forced with the large-scale conditions on two of the observational days (section 3c). Ideally, the observations and simulations would cover the same days. Unfortunately, many days of observations are needed to get statistically meaningful results, and, of those days, the simulations were deemed sufficiently faithful to the observations (in terms of cloud depth, cloud fraction, and liquid water path) on only two of them. There is still value in comparing the observations and simulations—and, as we will find, there are some notable similarities and differences—but we must always bear in mind this important caveat.

a. Stereo photogrammetry

In August of 2017, a ring of six cameras was installed in Oklahoma to perform stereo reconstructions of shallow clouds (Romps and Öktem 2018). These cameras are situated along the perimeter of a 12-km-wide circle; the center of that circle lies at 36.605°N, 97.486°W, which is in middle of the Department of Energy (DOE) Atmospheric Radiation Measurement (ARM) Southern Great Plains (SGP) Central Facility (Mather and Voyles 2013). The cameras themselves sit well outside the Central Facility (6 km away), facing back toward the center. Using stereo-photogrammetric reconstruction, the images from these cameras are used to produce the Clouds Optically Gridded by Stereo product (COGS; Romps and Öktem 2018). COGS data consist of an array of binary values (cloudy or clear) on a grid of 50 m in each of three spatial dimensions (over a cubic domain 6 km wide) and 20 s in time. The camera ring has been in operation since August 2017 with a 90% uptime, and the production of COGS is triggered on days with shallow cumulus, which leads to about 50 days of COGS data per year. When a cloud forms before it drifts into the 6-km-wide COGS domain

and/or decays after it has left the COGS domain, we track the cloud using one or more of the cameras to identify the times when the first fragment of the cloud appears and/or the last vestige disappears; these are referred to henceforth as the cloud's birth and death, respectively.

We identified 12 days from fall 2017 to summer 2018 when shallow cumulus was the only low cloud type present throughout the day.[1] On each of those days, we tracked clouds that maximized their volume inside the COGS domain, had a total lifetime (inside and outside the COGS domain) of at least five minutes, and had a nonzero basal area (see the definition of the cloud base below), and were clearly visible to at least one camera at the moments of birth and death. Clouds were identified and tracked in the COGS data (and in the LES data described below) using the vertically projected cloudiness (i.e., a two-dimensional grid of binary values indicating whether or not there is any cloud in the corresponding column). A representative set of clouds were selected for tracking, all of which satisfied a set of conditions regarding merging and splitting. These conditions are as follows. If a cloud of comparable size to the tracked cloud touches the tracked cloud (i.e., they form a single contiguous area of cloudiness), they must remain contiguous for no more than three minutes and there must be an obvious and reasonable way to draw a boundary between them using the three-dimensional data during that time. If a cloud of comparable size merges with the tracked cloud in the first eighth of their lifetimes, they must remain merged thereafter. If the tracked cloud splits into two or more parts, the area of the largest part must be 80% or more of the sum of all the areas of the parts, and only those parts that have an edge less than 150 m from an edge of the largest part are considered to still belong to the tracked cloud.

This procedure generated 3 tracked clouds on the lowest-yielding day and 42 on the highest-yielding day, for a total of 158 clouds across all days. Each cloud was tracked frame by frame by a human from birth (first moment of any associated cloudiness) to death (last moment of any associated cloudiness) using a combination of COGS and raw camera imagery. As a shorthand, we will refer to the resulting life cycle dataset, along with the associated Doppler lidar data described below, as OBS. Using the OBS dataset, the value of V_{max} for each cloud is simply the largest instantaneous volume that it achieves while in the COGS domain.

Since COGS does not measure gridpoint velocities, we cannot use it to calculate V_{up} and V_{down}. On the other hand, we can use COGS to calculate cloud-base areas. A simple definition of a cloud's instantaneous ''cloud base'' would be the set of each column's lowest horizontal face of the cloud. This has the potential to include, however, many cloud surfaces that are well above the cloud's initial LCL. Therefore, we wish to define ''cloud base'' for each cloud as only those lowest horizontal faces that are below some threshold height suitably close to the LCL of near-surface air. Since that LCL evolves throughout

---

[1] The 12 dates are 3 September 2017, 4 May 2018, 14 May 2018, 16 May 2018, 17 May 2018, 22 May 2018, 23 May 2018, 29 May 2018, 30 May 2018, 6 June 2018, 4 July 2018, and 13 July 2018.

the day, and since the cloud-base height of an individual cloud can deviate somewhat from the near-surface-air LCL height, we define the threshold height separately for each cloud as 100 m above the lowest 5th percentile of its grid points from all times it is within the COGS domain.

b. Doppler lidar

The COGS domain is intentionally centered on the vertically pointing Doppler lidar at the SGP Central Facility, and that lidar can be used to measure cloud-base vertical velocities. Since the lidar measures only a few places and times on any individual cloud, its measurements must be aggregated across multiple clouds and multiple days to get accurate measures of the ascending and descending cloud-base fluxes. We must also ensure that we are measuring vertical velocities at the "cloud base" defined in terms of the threshold heights. This is accomplished as follows. For each cloud in OBS, we examine the lidar data for 10 min before and 10 min after the cloud passes closest to the center of the COGS domain. The lidar is programmed to sample the overlying column every 3 s (except in 2017, when the sampling period was 1.5 s) with a vertical resolution of 30 m. A return signal from the lidar is determined to be from cloudy air if the attenuated backscatter exceeds $6 \times 10^{-5} \, \text{m}^{-1} \, \text{sr}^{-1}$. For every lidar sample in that 20-min interval, we collect the vertical velocity of the lowest cloudy point, if any, that is below the corresponding cloud's threshold height, which would make that vertical velocity a sample from the "cloud base." This generates a set of 3774 cloud-base vertical velocities. An alternative method was tried in which lidar data were collected only when the corresponding COGS cloud was overhead, but that only reduced the number of samples without otherwise affecting the results.

c. Large-eddy simulations

The LES ARM Symbiotic Simulation and Observation library (LASSO; Gustafson et al. 2020) is a collection of large-eddy simulations performed with the initial conditions and large-scale forcings corresponding to days of shallow cumulus at the SGP Central Facility. Of the 12 dates included in the OBS dataset, we identified two simulations (one on 6 June 2018 and one on 4 July 2018) that matched the diurnal variation in cloud liquid-water path during the study period (i.e., the cloud thicknesses closely matched observations) and that also agreed well with the horizontal cloud fraction from COGS and the total-sky imager.[2] We then reran two pairs of those LASSO simulations so that we could output three-dimensional snapshots of the atmosphere every 20 s. These simulations used the Weather Research and Forecasting (WRF) Model (Skamarock et al. 2008) modified for flexible LES configurations (Endo et al. 2015) with a horizontal grid spacing of 100 m, a vertical grid

---

[2] We used the large-scale forcing based on the VARANAL product for 6 June 2018 (LASSO simulation ID 2) and the ECMWF forecast with medium-scale domain for 4 July 2018 (simulation ID 5). The ECMWF simulation used is an earlier version of the forcing for which the large-scale vertical velocity is one-tenth of the final version in the ARM archive.

spacing of 30 m below 5 km, a horizontal domain size of 14.4 km, and a model top at 15 km. The physics suite included the Rapid Radiative Transfer Model for general circulation models radiation scheme (RRTMG; Iacono et al. 2008) and a 1.5-order subgrid-scale turbulence scheme (Deardorff 1980). The simulations were initialized with a sounding profile at 1200 UTC (0600 local time) and were driven for 15 h by prescribed surface fluxes from the ARM Variational Analysis product (VARANAL; Xie et al. 2004).

The first pair of simulations (one for 6 June and one for 4 July) used the Thompson microphysics scheme (Thompson et al. 2008), which uses saturation adjustment to enforce thermodynamic equilibrium between the water vapor and cloud droplets, if any. The second pair of simulations were run for the same dates, but differed in two respects: they used the Hebrew University fast spectral-bin microphysics scheme (HUJI; Khain et al. 2010), in which the droplet size distribution is simulated using 33 mass bins; and they included a representation of the horizontal longwave radiative flux emitted from cloud sides as implemented in Endo et al. (2019) following Guan et al. (1997).

To generate a binary cloud mask similar to COGS, each gridpoint is defined as clear or cloudy using a threshold condensate mass fraction of 10^{-5}. In each of these simulations, we then tracked 35 clouds frame by frame from birth to death (for a total of 140 clouds) with the same methodology applied to the COGS data. As a shorthand, the resulting life cycle datasets will be referred to here as STD (for the two simulations with standard microphysics) and SBM (for the two simulations with spectral bin microphysics). The value of V_{max} for each cloud is simply the largest instantaneous volume that it achieves over its entire lifetime. The instantaneous basal surface of each cloud is defined in the same way as with COGS: a threshold height is defined for each cloud as 100 m above the lowest 5th percentile of the cloud over its lifetime, and the cloud's base in each moment and column is its lowest cloud–clear interface below that threshold height, if any.

Since the simulation output has vertical velocity, it is straightforward to calculate a cloud's V_{up} and V_{down} as the integrated ascending volume flux and descending volume flux, respectively, over its basal surface over its lifetime. In practice, denoting the vertical velocity by w and the Heaviside unit step function by $\mathcal{H}$, V_{up} can be calculated as the sum of $w\mathcal{H}(w)$ at all of the cloud's basal gridpoint interfaces from all of the output snapshots multiplied by both the square of the horizontal grid spacing and the time interval between snapshots. Likewise, V_{down} is calculated using $-w\mathcal{H}(-w)$.

To confirm that the simulations are producing clouds whose scales match those of the observations, Fig. 2 gives the probability density functions of clouds within the three datasets (OBS, STD, and SBM; black, solid blue, and dashed blue, respectively) with respect to four different measures (the four panels) of cloud size or lifetime. Since each dataset has $O(100)$ clouds (158 in OBS and 70 in each of STD and SBM), the distributions are somewhat noisy. Nevertheless, the distributions are quite similar between the three datasets. The median values, indicated by the arrows in Fig. 2, fall within 240 ± 20 m for the maximum effective radius (the square root of maximum
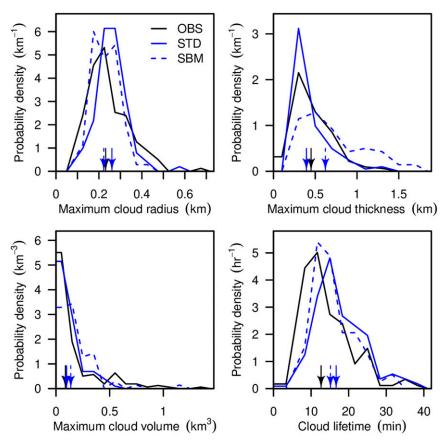
FIG. 2. The distributions of individual clouds among the datasets of OBS (black), STD (solid blue), and SBM (dashed blue) as functions of the cloud's (top left) maximum effective radius, (top right) maximum thickness, (bottom left) maximum volume, and (bottom right) lifetime. The curves for STD and SBM are generated from 70 clouds (35 for 6 Jun 2008 and 35 for 4 Jul 2008) and the curves for OBS are generated from 158 clouds collected over 12 different days. Arrows indicate the median values.

cloud-base area divided by π), 500 ± 100 m for the maximum thickness, 0.11 ± 0.03 km^3 for the maximum volume, and 15 ± 2 min for the lifetime.

4. Life cycle of radius and envelope

To get a sense for the cloud life cycle, we can build a composite as follows. For each snapshot of each cloud in each of the three datasets (STD, SBM, and OBS), we calculate an effective cloud-base radius as the square root of the basal area divided by π. Dividing that effective radius by the maximum effective radius over the cloud's lifetime gives a normalized radius. Let us also define a normalized time equal to zero at the cloud's birth and one at the cloud's death, both as recorded by the cameras. For the OBS dataset, most clouds will either be born or die outside the COGS domain, so there are some missing data, but we know that the normalized radius is zero at the times of birth and death. For each cloud in each of the datasets, we interpolate its normalized radius to 100 equally spaced times from 0 to 1 and plot the resulting value as a dot in Fig. 3. For OBS, the dots occurring at times outside the COGS

domain are colored red. The reason why some clouds reach a normalized radius of zero before their death is because the basal surface area goes to zero while there is still some remnant cloud above the threshold height. In each panel, the solid curve goes through the mean of the normalized radius at each time.

The observational results in the right panel of Fig. 3 show that the clouds are not behaving anything like pure plumes. The time series of effective radius for a plumelike cloud would have a long plateau corresponding to an approximate steady-state condition. Here, we see from the mean of the data (the black curve) that there is no such plateau. Any appearance of a plateau at a normalized radius of one in the samples of individual clouds (the points) is simply a visual artifact of the normalization: by definition, every cloud hits exactly one at some point in its life cycle. We can quantify the absence of a plateau by comparing the distribution of the normalized radii from all clouds to the distribution of $\sin(\phi)$ for ϕ evenly sampled from 0 to π. The distributions are nearly identical: the values at the 25th, 50th, and 75th percentiles for the normalized radii (sine function) are 0.34 (0.38), 0.68 (0.71), and 0.90 (0.92), respectively. Note that the STD and SBM datasets (left and
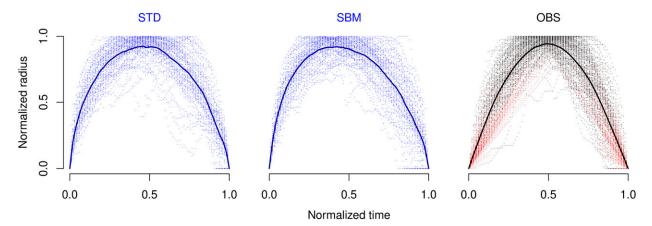
FIG. 3. Normalized effective radius of cloud base (dots) plotted as a function of normalized time for each of the clouds in the (left) STD, (center) SBM, and (right) OBS datasets. The panels for STD and SBM each show data from 70 clouds (35 for 6 Jun 2008 and 35 for 4 Jul 2008) and the panel for OBS shows data from 158 clouds collected over 12 different days. The solid curves plot the mean normalized radius. The red dots in the OBS panel are linear extrapolations during times when a cloud is outside the COGS domain toward the beginning and/or end of its life cycle.

middle panels) agree on the absence of a plateau: their normalized time series broadly agree with that of OBS. Note, however, that while this absence of a plateau allows us to rule out $B \ll 1$, it does not otherwise constrain the average value of B.

Next, we can define a normalized height for each cloud that goes from zero at the height of the lowest gridpoint over its lifetime to one at its highest gridpoint over its lifetime. Time series of the normalized height of the lowest point on the cloud are then interpolated to the 100 normalized times and plotted as dots in each of the panels of Fig. 4. The highest point on the cloud is plotted likewise, and the means of the normalized cloud bottoms and cloud tops are plotted as solid curves. For OBS, only times occurring within the COGS domain are included. The broad features of these time series are remarkably consistent across the three datasets: the cloud-top height rises up and sinks back down as the base undulates relatively little, but the base of the cloud tends to rise up at the end of the life cycle such that the final remnants of the cloud are aloft. The

fact that some of the cloud tends to dissipate above the cloud base tells us that these shallow cumulus clouds are at least partially active.

5. Values of *F* and *B*

The STD and SBM datasets each contain 70 triplets of V_{up}, V_{down}, and V_{max}, from which 70 pairs of F and B can be calculated. These (F, B) pairs are plotted in the left and center panels of Fig. 5 with the area of each circle proportional to V_{up}. Note that the four corners of these plots correspond to the four extremal cases depicted in Fig. 1. For both STD and SBM, most of the clouds are more active than forced, which means that most of the cloudy air dissipates above the cloud base instead of sinking back down through the cloud base. We also see that most of the clouds are in between a plume and a bubble; for example, $B = 0.5$ implies that the maximum instantaneous cloud volume is only half of the volume that ascends through the cloud base over the cloud's lifetime.
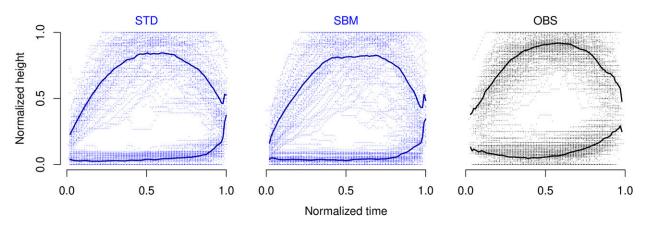

FIG. 4. As in Fig. 3, but for the normalized envelope of the clouds.
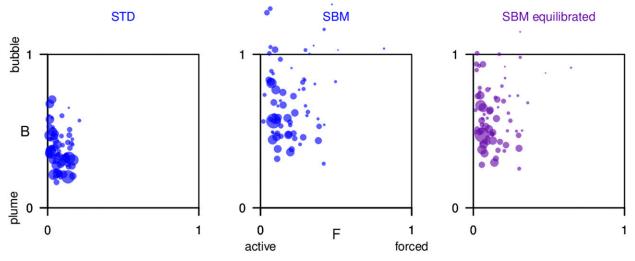
FIG. 5. Individual clouds plotted on axes of F and B for (left) STD, (center) SBM, and (right) SBM with thermodynamically equilibrated air, all with cloudy defined as a condensate mass fraction greater than 10^{-5}. The area of each circle is proportional to the cloud's V_{up}; the largest circle has a V_{up} of about 2 km^3.

Although the STD and SBM datasets broadly agree on these two points [(i) more active than forced, (ii) in between plume and bubble], there are obvious differences between the two datasets as well. Using the spectral microphysics has generally increased the F value of the clouds, making them somewhat more forced. This phenomenon was first documented by Endo et al. (2019). Another difference is that the spectral microphysics makes the clouds more bubble-like, with 12 of the 70 clouds having $B > 1$. These differences in F and B are caused, in part, by the finite time scale of evaporation when using a spectral scheme. This finite time scale leads to extra cloudiness at a cloud's periphery: with the same pressure, water content, and moist static energy, much of that periphery would be clear air if forced to equilibrate thermodynamically, as is the case in a standard scheme with instantaneous saturation adjustment. To prove this point, the right panel of Fig. 5 recalculates F and B for each of the SBM clouds after thermodynamically equilibrating all of the grid boxes in the snapshots (i.e., evaporating liquid water as needed to achieve saturation). Doing so reduces both F and B, nearly eliminating all cases with $B > 1$.

a. Comparison with OBS

Are the F and B values obtained from the large-eddy simulations consistent with observations? Unfortunately, there is no way to calculate B for a *single* cloud from observations because doing so would require having the vertical-velocity field over the cloud's basal surface for its entire lifetime, which is not possible with current instruments. On the other hand, we can calculate an ensemble-mean B from OBS using multiple days so as to get a result with a useful confidence interval. Let us first define the effective ascent rate w_{up} through a cloud's base as

$$w_{up} = \frac{\int dt \int_{cb} dx\, dy\, w_{cb} \mathscr{H}(w_{cb})}{\int dt \int_{cb} dx\, dy}, \tag{3}$$

where $\int_{cb(t)}$ is an integral over the cloud base at time t, $w_{cb}(x, y, t)$ is the cloud-base vertical velocity, and $\mathscr{H}$ is the Heaviside unit step function. For notational simplicity, we can write the instantaneous basal area as $A_{cb} = \int_{cb} dx\, dy$. With these definitions, we can write V_{up} as

$$V_{up} = w_{up} \int dt\, A_{cb}. \tag{4}$$

If w_{up} is independent of cloud size, then we can replace w_{up} with an average value $\overline{w}_{up}$ (e.g., from several days of lidar data) when calculating an ensemble mean of V_{up} for many clouds. Figure 6 plots V_{up} versus $\int dt\, A_{cb}$ for all 140 of the clouds in
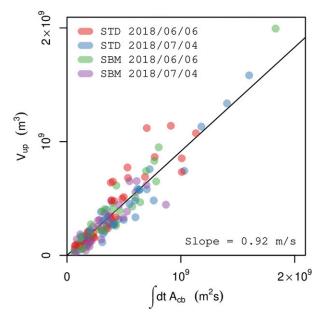

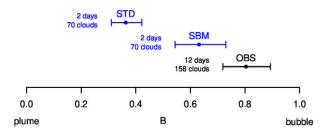FIG. 6. Individual LES clouds plotted on axes of V_{up} and $\int dt\, A_{cb}$.

FIG. 7. V_{up}-weighted ensemble-mean B using $\overline{w}_{up}$. Circles are means and whiskers show the 95% confidence interval.

FIG. 8. V_{up}-weighted ensemble-mean F. Circles are means and whiskers show the 95% confidence interval.

STD and SBM. The fact that the clouds cluster along a single line that goes through the origin means that we can, indeed, use $\overline{w}_{up}$ in place of w_{up} when calculating ensemble means.[3]

We can calculate $\overline{w}_{up}$ from the STD and SBM data as

$$\overline{w}_{up} = \frac{\sum_i V_{up,i}}{\sum_i \int dt\, A_{cb,i}} = 0.92 \text{ m s}^{-1} \quad (95\% \text{ CI } [0.87, 0.96])$$

$$\text{(STD and SBM).} \tag{5}$$

This slope is plotted as the solid line in Fig. 6. We can calculate $\overline{w}_{up}$ from OBS using the lidar measurements from all 12 observational days. Indexing each cloud-base vertical-velocity measurement with an i, which ranges from 1 to $N = 3774$, $\overline{w}_{up}$ is calculated as

$$\overline{w}_{up} = \frac{1}{N}\sum_i w_i \mathscr{H}(w_i) = 0.70 \text{ m s}^{-1} \quad (95\% \text{ CI } [0.67, 0.73])$$

$$\text{(OBS).} \tag{6}$$

In both of the preceding equations, the confidence intervals are calculated using bootstrapping. For STD and SBM, clouds are selected randomly with replacement to generate 10 000 sets of $V_{up,i}$ and $A_{cb,i}$ from which 10 000 realizations of $\overline{w}_{up}$ are calculated. For OBS, the cloud-base vertical velocities are strung together in order and a sets of w_i are generated by sampling blocks of a mean length of 50 (this length was determined from an autocorrelation analysis, although the results are not very sensitive to that choice).

Replacing w_{up} with $\overline{w}_{up}$ in (4), we can write the V_{up}-weighted ensemble mean of B as

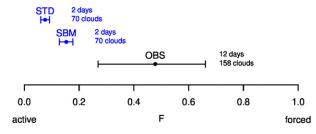$$B = \frac{\sum_i V_{max,i}}{\overline{w}_{up} \sum_i \int dt\, A_{cb,i}}. \tag{7}$$

To generate a confidence interval for B, we bootstrap 10 000 samples of paired sets of $V_{max,i}$ and $A_{cb,i}$ and match those with 10 000 bootstrapped samples of $\overline{w}_{up}$. Figure 7 shows the results with whiskers showing the 95% confidence interval. We see that the B values reported by STD, SBM, and OBS are all different with statistical significance. OBS reports a mean B of 0.80 for the 12 days of observations while STD and SBM report smaller values for their two days of 0.36 and 0.63, respectively. In other words, the observed clouds behave mostly like bubbles while the clouds in the simulations are, on average, more intermediate between a plume and bubble. It is noteworthy, however, that SBM is closer to the observations than STD.

To compare F between simulations and observations, we can use the lidar data to calculate the V_{up}-weighted ensemble-mean F from observations as

$$F = \frac{\sum_i -w_i \mathscr{H}(-w_i)}{\sum_i w_i \mathscr{H}(w_i)} \quad \text{(OBS).} \tag{8}$$
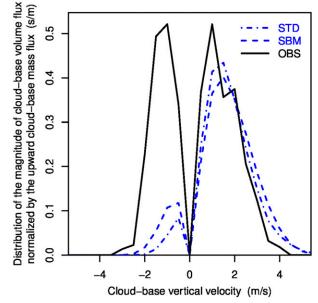

FIG. 9. Normalized distributions of the magnitude of cloud-base volume flux for STD (dashed–dotted blue), SBM (dashed blue), and OBS (solid black). Each distribution has been normalized by the integral over positive cloud-base vertical velocity (i.e., normalized by the gross ascending volume flux).

---

[3] Recent work with a vertically pointing Doppler lidar has shown that larger cloud-base chords tend to have a higher mean vertical velocity (Lareau et al. 2018; Griewank et al. 2020), but this does not imply that larger cumuli have, on average, a higher vertical velocity. In fact, a positive correlation between chord length and vertical velocity would be expected in the absence of any correlation between cloud size and vertical velocity: shorter chords tend to be sampled from the edges of clouds, which have a lower vertical velocity than the cloud center.
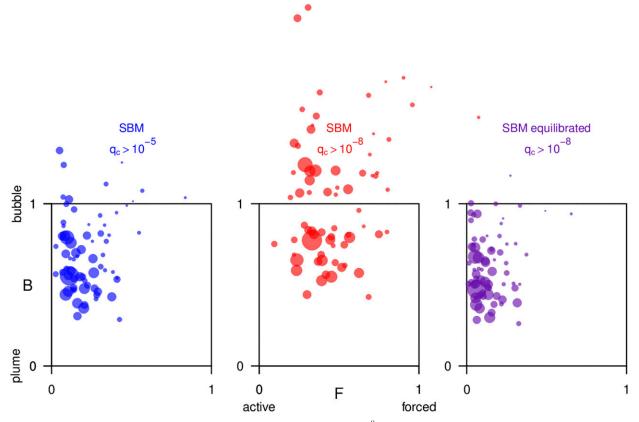
FIG. 10. As in Fig. 5, but identifying individual clouds using a q_c threshold of 10^{-8} and then calculating F and B using the cloud boundaries defined by a threshold of (left) 10^{-5}, (center) 10^{-8}, and (right) 10^{-8} after thermodynamically equilibrating each grid cell in each snapshot.

Likewise, for the simulations, we can calculate the V_{up}-weighted ensemble-mean F as

$$F = \frac{\sum_i V_{down,i}}{\sum_i V_{up,i}} \quad \text{(STD and SBM)}. \qquad (9)$$

Confidence intervals are calculated as before with boot-strapped sets of w_i for OBS and bootstrapped sets of clouds for STD and SBM. Figure 8 shows the results. The three datasets give different results with statistical significance. The observed clouds are intermediate between active and forced (with a mean F of 0.48) while the simulated clouds are much more active (with a mean F of 0.08 for STD and 0.15 for SBM), echoing the conclusions of Endo et al. (2019).

Another way to see that the clouds in the simulations are much more active is to plot histograms of the cloud-base vertical volume fluxes. Figure 9 shows the histograms of the magnitude of vertical volume flux binned by vertical velocity and normalized by the integral of the ascending flux. We see that clouds in STD and SBM have far less cloudy air descending at the cloud base. While it is important to bear in mind the caveat that 12 days of observations are being compared to only 2 days of simulations, the differences exhibited in this histogram are stark and unlikely to stem from sampling bias considering that the clouds are otherwise very similar (as seen

in Figs. 2–4). The same can be said of the large discrepancies between STD and OBS with regards to F (≈ 0.08 and ≈ 0.5, respectively) and B (≈ 0.4 and ≈ 0.8, respectively).

b. Sensitivity to the condensate threshold

In the preceding sections, we have used data of multiple different types. One of the difficulties in comparing these datasets is that they all use different definitions of clear and cloudy: for the large-eddy simulations, clouds are identified based on a threshold of condensate mass fraction; for the stereo cameras, an algorithms determines cloud boundaries based on visible matching features; for the Doppler lidar, clouds are identified based on the attenuated backscatter exceeding $6 \times 10^{-5} \, m^{-1} \, sr^{-1}$. To show that results can be sensitive to these choices, we recalculate the SBM dataset from scratch using a condensate threshold of 10^{-8} instead of the threshold of 10^{-5} used in the preceding sections. Once the clouds have been identified and tracked using that threshold, we then tighten the threshold back to 10^{-5} to recalculate F and B for each of the clouds, the result of which is shown in the left panel of Fig. 10. Since these clouds were first identified and tracked using the 10^{-8} threshold, the details are slightly different from the middle panel of Fig. 5, but the distribution is broadly the same.

On the other hand, the middle panel of Fig. 10, which uses the 10^{-8} threshold, is quite different. Using this lower threshold adds an additional periphery to the cloud that adds to the

downward flux at cloud base (increasing V_{down}) and increases the cloud volume (increasing V_{max}). These effects increase F and B, respectively. In fact, this lower condensate threshold increases the average F to around 0.5, consistent with the observations in Fig. 8. But B increases by so much that half of the clouds have a B greater than one, and many by a large margin. As discussed earlier, the nonconservation of cloud volume due to entrainment is expected to be less than or equal to about 10%, so entrainment cannot explain these large values of B. Instead, the root cause of the high B values is the large volume of cloudy air that would be clear air if equilibrated. The right panel of Fig. 10 shows the F and B values using the same threshold of 10^{-8}, but first equilibrating each grid cell thermodynamically. Enforcing thermodynamic equilibrium reduces both F and B and eliminates nearly all the cases of $B > 1$, yielding a result similar to the right panel of Fig. 5.

We see that F and B depend critically on the condensate threshold used to define cloudy air, but what condensate threshold is "right"? There is, of course, no unique answer to this question, but it is worth noting that a threshold of 10^{-8} is very small. Assuming a monodisperse collection of cloud droplets with a typical continental concentration of $1000\,cm^{-3}$, a mass fraction of $q_c = 10^{-8}$ would imply a droplet radius of $0.1\,\mu m$. That is a size typical of aerosols, not activated cloud drops.

6. Summary

We have introduced definitions of forced, active, plume, and bubble that allow us to calculate the degree to which a cloud exhibits these properties. As defined in Eqs. (1) and (2), F ranges from 0 (for purely active) to 1 (for purely forced) and B ranges from 0 (for a pure plume) to 1 (for a pure bubble). With the use of large-eddy simulations, stereo photogrammetry, and Doppler lidar, we find differences between the observations and the simulations. The observations indicate that the shallow cumulus clouds typical of Oklahoma are largely bubble-like ($B \approx 0.8$) and are intermediate between active and forced ($F \approx 0.5$). The simulations, on the other hand, produce clouds that are substantially more plumelike and active. An important caveat, however, is that we have compared an average of observations over 12 days with an average over large-eddy simulations on only two of those days. We have also found that two choices can have a material impact on the values of F and B obtained from large-eddy simulations: the choice of microphysics scheme and the condensate threshold used to distinguish cloudy air from clear.

APPENDIX

Maximum Puff Factor

The volume to which a cloud can grow by entrainment is limited by the amount of environmental air that can be incorporated to exactly evaporate the cloud's droplets. For simplicity, let us assume that a parcel of cloudy air has the same temperature as its clear-air environment. Let q_v be the mass fraction of water vapor in the environment and let q_v^* be the saturation value, which is also the mass fraction of water vapor in the cloud. Relative humidity is usually defined as a ratio of partial pressures, but a good approximation for the relative humidity of the environmental air is $RH = q_v/q_v^*$. To exactly evaporate 1 kg of cloudy air with ξ kg of clear air, we need

$$(1 + \xi)h^*(T_f) = h^*(T_i) + \xi h_e(T_i), \tag{A1}$$

$$(1 + \xi)q_v^*(T_f) = q_v^*(T_i) + q_l + \xi RH q_v^*(T_i), \tag{A2}$$

where T_i and T_f are the parcel's initial and final temperatures (before and after entrainment), h^* and h_e are the moist static energies (MSE) of the parcel and the environment, and q_l is the initial mass fraction of liquid in the cloud. These equations state the conservation of MSE and water, with the final state being saturated with no condensate.

Using the Clausius–Clapeyron relation and assuming that this process occurs at constant height and pressure, we can solve for ξ to get

$$\text{maximum puff factor} \equiv 1 + \xi \approx 1 + \left[1 + \frac{L^2}{c_p R_v T^2} q_v^*\right] \times \frac{q_l}{(1 - RH)q_v^*}, \tag{A3}$$

where L is the specific latent heat of evaporation, c_p is specific heat capacity of air at constant pressure, and R_v is the specific gas constant. This is the maximum factor by which the cloud can be made larger in mass by entrainment; the volumetric factor will be slightly less due to the cloud's colder temperature, but that effect is less than 1%, which can be safely ignored, so we can apply this maximum puff factor to volume as well. Taking a snapshot of one of the large-eddy simulations with 96 clouds present, we calculate the maximum possible puffing of each cloud using the actual q_l in each of its grid boxes and the mean RH of clear air in the domain at those heights. This gives 96 maximum puff factors for each of the 96 clouds, which have a mean value of 1.19 and a standard deviation of 0.06.

REFERENCES

Chen, T., W. B. Rossow, and Y. Zhang, 2000: Radiative effects of cloud-type variations. *J. Climate*, **13**, 264–286, https://doi.org/10.1175/1520-0442(2000)013<0264:REOCTV>2.0.CO;2.

Dawe, J. T., and P. H. Austin, 2011: Interpolation of LES cloud surfaces for use in direct calculations of entrainment and detrainment. *Mon. Wea. Rev.*, **139**, 444–456, https://doi.org/10.1175/2010MWR3473.1.

Deardorff, J. W., 1980: Stratocumulus-capped mixed layers derived from a three-dimensional model. *Bound.-Layer Meteor.*, **18**, 495–527, https://doi.org/10.1007/BF00119502.

Endo, S., and Coauthors, 2015: RACORO continental boundary layer cloud investigations: 2. Large-eddy simulations of cumulus clouds and evaluation with in situ and ground-based observations. *J. Geophys. Res. Atmos.*, **120**, 5993–6014, https://doi.org/10.1002/2014JD022525.

——, and Coauthors, 2019: Reconciling differences between large-eddy simulations and Doppler-lidar observations of continental shallow cumulus cloud-base vertical velocity. *Geophys. Res. Lett.*, **46**, 11 539–11 547, https://doi.org/10.1029/2019GL084893.

Griewank, P. J., T. Heus, N. P. Lareau, and R. A. J. Neggers, 2020: Size dependence in chord characteristics from simulated and observed continental shallow cumulus. *Atmos. Chem. Phys.*, **20**, 10 211–10 230, https://doi.org/10.5194/acp-20-10211-2020.

Guan, H., M. K. Yau, and R. Davies, 1997: The effects of longwave radiation in a small cumulus cloud. *J. Atmos. Sci.*, **54**, 2201–2214, https://doi.org/10.1175/1520-0469(1997)054<2201:TEOLRI>2.0.CO;2.

Gustafson, W. I., and Coauthors, 2020: The Large-eddy simulation (LES) Atmospheric Radiation Measurement (ARM) Symbiotic Simulation and Observation (LASSO) activity for continental shallow convection. *Bull. Amer. Meteor. Soc.*, **101**, E462–E479, https://doi.org/10.1175/BAMS-D-19-0065.1.

Iacono, M. J., J. S. Delamere, E. J. Mlawer, M. W. Shephard, S. A. Clough, and W. D. Collins, 2008: Radiative forcing by long-lived greenhouse gases: Calculations with the AER radiative transfer models. *J. Geophys. Res.*, **113**, D13103, https://doi.org/10.1029/2008JD009944.

Khain, A., B. Lynn, and J. Dudhia, 2010: Aerosol effects on intensity of landfalling hurricanes as seen from simulations with the WRF Model with spectral bin microphysics. *J. Atmos. Sci.*, **67**, 365–384, https://doi.org/10.1175/2009JAS3210.1.

Lareau, N. P., Y. Zhang, and S. A. Klein, 2018: Observed boundary layer controls on shallow cumulus at the ARM Southern Great Plains site. *J. Atmos. Sci.*, **75**, 2235–2255, https://doi.org/10.1175/JAS-D-17-0244.1.

Mather, J. H., and J. W. Voyles, 2013: The ARM Climate Research Facility: A review of structure and capabilities. *Bull. Amer. Meteor. Soc.*, **94**, 377–392, https://doi.org/10.1175/BAMS-D-11-00218.1.

McCarthy, J., 1974: Field verification of the relationship between entrainment rate and cumulus cloud diameter. *J. Atmos. Sci.*, **31**, 1028–1039, https://doi.org/10.1175/1520-0469(1974)031<1028:FVOTRB>2.0.CO;2.

Romps, D. M., 2010: A direct measure of entrainment. *J. Atmos. Sci.*, **67**, 1908–1927, https://doi.org/10.1175/2010JAS3371.1.

——, and R. Öktem, 2018: Observing clouds in 4D with multiview stereophotogrammetry. *Bull. Amer. Meteor. Soc.*, **99**, 2575–2586, https://doi.org/10.1175/BAMS-D-18-0029.1.

Scorer, R. S., and F. H. Ludlam, 1953: Bubble theory of penetrative convection. *Quart. J. Roy. Meteor. Soc.*, **79**, 94–103, https://doi.org/10.1002/qj.49707933908.

Siebesma, A. P., and A. A. M. Holtslag, 1996: Model impacts of entrainment and detrainment rates in shallow cumulus convection. *J. Atmos. Sci.*, **53**, 2354–2364, https://doi.org/10.1175/1520-0469(1996)053<2354:MIOEAD>2.0.CO;2.

Skamarock, W. C., and Coauthors, 2008: A description of the Advanced Research WRF version 3. NCAR Tech. Note NCAR/TN-475+STR, 113 pp., https://doi.org/10.5065/D68S4MVH.

Stull, R. B., 1985: A fair-weather cumulus cloud classification scheme for mixed-layer studies. *J. Climate Appl. Meteor.*, **24**, 49–56, https://doi.org/10.1175/1520-0450(1985)024<0049:AFWCCC>2.0.CO;2.

Thompson, G., P. R. Field, R. M. Rasmussen, and W. D. Hall, 2008: Explicit forecasts of winter precipitation using an improved bulk microphysics scheme. Part II: Implementation of a new snow parameterization. *Mon. Wea. Rev.*, **136**, 5095–5115, https://doi.org/10.1175/2008MWR2387.1.

Turner, J. S., 1962: The 'starting plume' in neutral surroundings. *J. Fluid Mech.*, **13**, 356–368, https://doi.org/10.1017/S0022112062000762.

Xie, S., R. T. Cederwall, and M. Zhang, 2004: Developing long-term single-column model/cloud system-resolving model forcing data using numerical weather prediction products constrained by surface and top of the atmosphere observations. *J. Geophys. Res.*, **109**, D01104, https://doi.org/10.1029/2003JD004045.

Yates, A. H., 1953: Atmospheric convection; the structure of thermals below cloud-base. *Quart. J. Roy. Meteor. Soc.*, **79**, 420–424, https://doi.org/10.1002/qj.49707934115.